frontiers in Earth Science

ORIGINAL RESEARCH
published: 10 December 2021
doi: 10.3389/feart.2021.742895

Implications of Multiple Disequilibrium Textures in Quartz-Hosted Embayments

Anna C. Ruefer[1,2]*, *Kenneth S. Befus*[1], *James O. Thompson*[1] and *Benjamin J. Andrews*[3]

[1]Geosciences Department, Baylor University, Waco, TX, United States, [2]Department of Geological Sciences, Stanford University, Palo Alto, CA, United States, [3]Global Volcanism Program, Smithsonian Institution, Washington, DC, United States

The faces of volcanic phenocrysts may be marked by imperfections occurring as holes that penetrate the crystal interior. When filled with glass these features, called embayments or reentrants, have been used to petrologically constrain magmatic ascent rate. Embayment ascent speedometry relies on the record of disequilibrium preserved as diffusion-limited volatile concentration gradients in the embayment glass. Clear, glassy embayments are carefully selected for speedometry studies. The use and subsequent descriptions of pristine embayments overrepresent their actual abundance. Here, we provide a textural analysis of the number, morphology, and filling characteristics of quartz-hosted embayments. We target a collection of large (i.e., >20 km^3 erupted volume) silicic eruptions, including the Bishop Tuff, Tuff of Bluff Point, Bandelier Tuff, Mesa Falls Tuff, and Huckleberry Ridge Tuff in the United States, Oruanui Tuff in New Zealand, Younger Toba Tuff in Indonesia, the Kos Plateau Tuff in Greece, and the Giant Pumice from La Primavera caldera in Mexico. For each unit, hundreds of quartz crystals were picked and the total number of embayment-hosting crystals were counted and categorized into classifications based on the vesicularity and morphology. We observed significant variability in embayment abundance, form, and vesicularity across different eruptions. Simple, cylindrical forms are the most common, as are dense glassy embayments. Increasingly complex shapes and a range of bubble textures are also common. Embayments may crosscut or deflect prominent internal cathodoluminescence banding in the host quartz, indicating that embayments form by both dissolution and growth. We propose potential additional timescales recorded by embayment disequilibrium textures, namely, faceting, bubbles, and the lack thereof. Embayment formation likely occurs tens to hundreds of years before eruption because embayment surfaces are rounded instead of faceted. Bubble textures in embayments are far from those predicted by equilibrium solubility. Homogenous nucleation conditions likely allow preservation of pressures much greater than magmastatic inside embayments. Our textural observations lend insight into embayment occurrence and formation and guide further embayment studies.

Keywords: embayments, silicic eruption, bubbles, rhyolite, reentrants, disequilibrium

OPEN ACCESS

Edited by:
Jacob B. Lowenstern, Cascades Volcano Observatory, United States

Reviewed by:
Alison Claire Rust, University of Bristol, United Kingdom
Rebecca deGraffenried, Ruhr-Universität Bochum, Germany

***Correspondence:**
Anna C. Ruefer
aruefer@stanford.edu

Specialty section:
This article was submitted to Volcanology, a section of the journal Frontiers in Earth Science

Received: *16 July 2021*
Accepted: *26 November 2021*
Published: *10 December 2021*

Citation:
Ruefer AC, Befus KS, Thompson JO and Andrews BJ (2021) Implications of Multiple Disequilibrium Textures in Quartz-Hosted Embayments. Front. Earth Sci. 9:742895. doi: 10.3389/feart.2021.742895

INTRODUCTION

Volcanic rocks preserve textures that reflect the dynamic magmatic and volcanic processes which lead to their formation, eruption, and preservation. The textures can be interpreted to infer processes in the subsurface that are not directly observable, including pre-eruptive magmatic storage, magmatic ascent, and fragmentation (e.g., Toramaru, 2006, 2008; Rutherford, 2008; Gardner et al., 2017). Some textures can be used as geospeedometers because they preserve information about the rates and timescales over which processes occur (e.g., Cashman, 1992; Pamukcu et al., 2015; Hajimirza et al., 2021).

Ascent rate exerts a primary control over eruptive style and explosivity (Hammer and Rutherford, 2002; Castro and Gardner, 2008; Castro and Dingwell, 2009; Cassidy et al., 2018). Glass-filled pockets in volcanic phenocrysts, called embayments or reentrants, have been exploited as a compositional, petrologic record of magmatic ascent, and have been increasingly applied as a geospeedometer for silicic and mafic systems (e.g., Liu et al., 2007; Humphreys et al., 2008; Lloyd et al., 2014; Ferguson et al., 2016; Myers et al., 2016, 2018, 2021; Moussallam et al., 2019; Newcombe et al., 2020). Embayments are parcels of melt which never become fully entrapped by the crystal host. The crystalline host shields the partially enclosed melt, presumably suppressing vesiculation and microlite nucleation. Upon erupting and quenching the embayment is preserved as a channel of glass. Embayments commonly occur in many minerals but most studies focus on quartz- or olivine-hosted embayments.

During ascent, shielded embayment melt experiences diffusion-limited equilibration of volatiles with the decompressing external magma. This diffusion-limited equilibration produces volatile gradients that can be used to recover magma decompression rates with numerical modeling (e.g., Liu et al., 2007; Myers et al., 2016; 2018; 2021; Georgeais et al., 2021). Successful modeling requires dense, glassy embayments, unmarred by bubbles or microlites. Simple shapes are also required for current models (deGraffenried and Shea, 2021). These requirements for geospeedometry may have resulted in a presumptive overrepresentation of the description of bubble-free embayments in the literature. Datasets are needed to constrain the existing unknowns about embayments, which range from embayment formation processes to their textural maturation. Embayments have been shown to be complex and multi-phased (e.g., Anderson, 1991, 2006; Liu et al., 2007; Cashman and Rust, 2016; Rust and Cashman, 2017). They may contain microlites, internal bubbles, and bubbles which extend from the exterior melt into the embayment glass. It remains unclear how common and consistent these textural complexities are from crystal to crystal, across different volcanic systems, and within individual eruptive units. These diverse textures may contain valuable additional previously unrecognized information about magmatic ascent and pre-eruptive conditions.

Here, we conduct a survey of textures present in quartz-hosted embayments from ten explosive, rhyolitic eruptions. We determine the abundance of embayments in quartz from each volcanic system. We then present the range of embayment morphologies and bubble textures within embayment glass. Based on these descriptions, we categorize embayment and embayment-hosted bubble morphologies and quantify the abundance of each morphology. We observe distinct variations in the number of crystals with embayments across the ten systems. Quartz crystals from some eruptions are nearly all embayed, whereas embayments are rare in other eruptions. Embayment morphologies are consistent within all eruptions, with simple, cylindrical forms as the dominant shape. Dense, glassy embayments without bubbles predominate, but bubble textures are also pervasive and diverse. Embayment textures contain additional information about embayment formation, magmatic storage, ascent processes and have implications for embayment geospeedometry. Specifically, we conclude that embayments may record independent timescales: the well-known volatile diffusion speedometer, a faceting timescale, and differences between homogeneous and heterogeneous nucleation revealed by bubble textures.

METHODS

Samples

Pumice samples were acquired from the Bishop Tuff of Long Valley caldera, Tuff of Bluff Point, Mesa Falls Tuff, and Huckleberry Ridge Tuff from Yellowstone caldera, Tsankawi Pumice of the Bandelier Tuff from Valles caldera, each in the United States, Oruanui Tuff from Taupo caldera in New Zealand, Younger Toba Tuff from Toba caldera in Indonesia, the Kos Plateau Tuff from the island of Kos in Greece, and the Giant Pumice from La Primavera caldera in Mexico (**Table 1**). These explosive, rhyolitic eruptions were specifically targeted because they are quartz-bearing and their locations span a range of geographic and tectonic environments. A representative population of 300–1,000 quartz crystals were handpicked from the 720 μm to 2 mm fraction of sieved pyroclastic material using a binocular microscope.

The nature of the pyroclastic source material varied by eruption because of availability. For the Tsankawi, Oruanui, Giant Pumice, and Huckleberry Ridge Tuff eruptions the quartz were picked from gently crushed air-fall pumice. Quartz were picked as loose crystals from crystal-rich air-fall deposits of the Bishop Tuff and Mesa Falls Tuff. Pumice from unwelded ignimbrites were the source of quartz for the Tuff of Bluff Point and Kos Plateau Tuff, and for a second assessment of the Bishop Tuff to compare with fall material. Densely welded ignimbrite was the best material we could acquire for the Younger Toba Tuff. We include the Younger Toba embayments in our study; however, we treat their interpretation with caution as processes in the ignimbrite (e.g., welding and slow cooling) likely modified the glass and bubble textures in the embayments. Because embayments extend from the crystal surface to the interior we restricted our analysis to crystals with >50% of their surface preserved and unbroken by processes during or after emplacement. In the majority of the eruptions, unbroken crystals were common and easy to select. In

TABLE 1 | Summary of data.

Volcano	Unit	Deposit	Mineral phases	Eruption age (Ma)	Erupted volume (km^3)	Previous decompression rate estimates ($MPa\ s^{-1}$)
Valles	Upper Bandelier Tuff	Tsankawi Pumice Fall	qtz, san, pyx, mgt, ap, hbl, bt, il	1.14	250	0.0021–0.022
Taupo	Oruanui	Fall (F1-2)	plag, qtz, opx, hbl, mgt, il	0.026	430	0.001–0.11
Kos	Kos Plateau Tuff	Ignimbrite (E)	plag, san, qtz, bt, il, mgt, mon, zr, ap	0.16	60	na
Yellowstone	Huckleberry Ridge Tuff	Fall	qtz, san, plag, cpx, fay	2.1	2,450	0.009–0.12
Yellowstone	Mesa Falls Tuff	Fall	qtz, san, plag, pyx, ox, zr	1.3	280	na
Yellowstone	Tuff of Bluff Point	Ignimbrite	qtz, san, plag	0.161	50	na
Long Valley	Bishop Tuff	Fall (F1-F3)	plag, san, bt, qtz	0.76	650	0.02–0.38
Long Valley	Bishop Tuff	Ignimbrite (Ig2Ea)	plag, san, bt, qtz	0.76	650	0.02–0.38
La Primavera	Giant Pumice	Lava dome	san, qtz, opx, fay, il, mgt	0.086	20	na
Toba	Younger Toba Tuff	Welded ignimbrite	qtz, san, plag, hbl, bt, opx, zr, mgt, il	0.074	2,800	na

Bandelier data from Saalfeld et al., 2019; Dunbar and Hervig, 1992.
Tuff of Bluff Point Data from Christiansen, 2001.
Bishop Tuff data from Hildreth and Wilson, 2007.
Giant Pumice data from Sourisseau et al., 2020.
Younger Toba Tuff data from Barbee et al., 2020.
Oruanui dara from Liu et al., 2006, 2007; Myers et al., 2018; Wilson et al., 2006.
Kos Plateau Tuff data from Bachmann et al., 2007.
Huckleberry Ridge Tuff data from Myers et al., 2018.
Mesa Falls Tuff data from Rivera et al., 2016.
"na" is unavailable data.

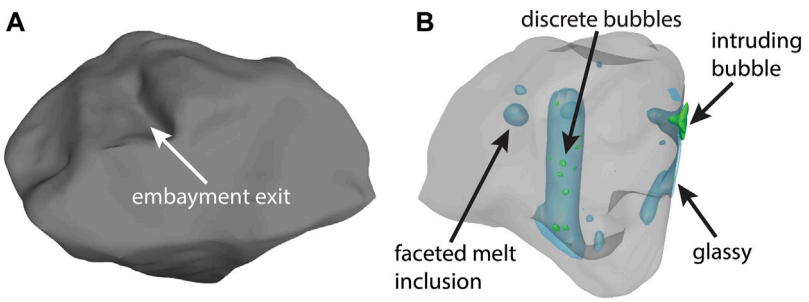

FIGURE 1 | (A) 3D tomography of a Bishop Tuff quartz crystal that hosts. **(B)** multiple glassy embayments with various bubble textures (gray = quartz, blue = glass, green = bubble). Tomography performed at μCT beamline 8.3.2 at the Advanced Light Source, Lawrence Berkeley National Laboratory and segmented using *Dragonfly*.

the Younger Toba Tuff, Oruanui Tuff, and Bishop Tuff most quartz occurred as fragments. Although our descriptions for these eruptions are robust because of high counts, we recognize that the relative proportion of textures may be diluted by too many crystal fragments.

Counting

The picked crystals were submerged in mineral oil, internally inspected, and separated into two groups: embayment-free and embayment-bearing. Each embayment-bearing crystal was further characterized based upon the morphology and degree of vesicularity of the embayment it hosts. The prevalence of specific embayment morphologies was counted. To quantify the occurrence of the embayment classes, we established a counting scheme based on the five observed categories for bubble textures and embayment geometries. Most crystals contained more than one embayment, but some contained dozens. Within a single crystal, it is common for up to three textural and morphological classes to occur simultaneously (**Figure 1**). To simplify our approach, only the first incidence of each texture or shape was counted for each individual crystal. For example, consider a single crystal with six embayments, three of which contained Texture A, 2 with Texture B, and 1 with Texture C. This crystal would count as "1" in the embayment-bearing category and "1" in each of the sub-categories: A, B, and C. We acknowledge that our approach establishes the relative abundance of embayment textures but does not quantify the absolute numbers. Multiple authors performed counts and textural analyses. To test reproducibility

TABLE 2 | Observed morphology percentages.

Morphology	Bandelier Tuff	Tuff of Bluff point	Huckleberry ridge	Giant pumice	Mesa falls Tuff	Kos plateau Tuff	Bishop Tuff (F1-F3)	Younger Toba Tuff
Simple	40	45	51	39	37	43	50	68
Bulbous	25	25	27	30	37	35	26	23
Hourglass	4	3	2	2	4	2	1	5
Bent	7	7	4	8	8	4	4	0
Complex	24	20	16	21	14	16	18	5
Embayed	85	82	71	69	53	49	55	4
N	302	720	228	425	497	453	106	22

between the authors, subsets of crystals from the same sample were independently categorized. Results from these tests produced differences less than 10%.

Cathodoluminescence (CL) Imagery

Quartz crystals from eight of the ten eruptions were selected for cathodoluminescence (CL) imagery (Kos Plateau Tuff and Oruanui Tuff were excluded). From each eruption, embayments of varying morphologies were selected, singly exposed, and polished. CL images were collected using the Smithsonian Institution JEOL JXA-8530FPlus HyperProbe Electron Probe Microanalyzer. Images were acquired with a focused 15 kV, 50 nA beam, with dwell times of 2–5 ms per pixel. The CL images were sized for nominal resolution of 0.5–1 μm pixel^{-1}, with image acquisition time ranging from 45–300 min.

RESULTS

The crystalline form of quartz varied by eruption. Most eruptions preserve collections of multiple forms occurring together, including beta quartz bipyramids, partial bipyramids, and rounded, anhedral grains. Quartz-hosted embayments are common features in all eruptions and all forms (**Table 2**; **Figure 2**). Rounded, anhedral crystals tend to contain more embayments than euhedral bipyramids. Embayment morphology varies widely and does not show a strong correlation with embayment or crystal size (**Table 2**). Morphologies were classified into five categories: simple, bulbous, bent, hourglass, and complex (**Figure 3**, **Figure 4**). Simple embayments are those ideal for embayment speedometry with near-perfect cylindrical geometry and little to no tapering of the outlet (Liu et al., 2007; deGraffenried and Shea, 2021). Bulbous embayments display a neck that tapers towards the outlet, extending from a rounded interior. Bent embayments exhibit a relatively simple symmetry near the outlet before a sharp 70–100° shift in direction, forming a hook-like geometry. Hourglass embayments, sometimes referred to as hourglass inclusions in the literature (e.g., Anderson, 1991; Lowenstern, 2003), are characterized by a thin, threadlike outlet connected to an interior bulb. Complex embayments are those which display any additional morphology. This category includes branching embayments and those that penetrate through the entire crystal. Embayment morphologies are notably similar across all eruptions in this study. The difference in proportions between embayment morphology categories is <15% for any given eruption or morphology (**Table 2**; **Figure 5**). The Younger Toba Tuff is an outlier, with a comparatively high proportion of embayments with a simple morphology (68%). Across all eruptions, simple embayments are the most common (37–51%), followed by bulbous (25–35%), complex (14–24%), bent (4–8%), and hourglass (1–4%).

Cross-cutting or deflecting relationships preserved by bands of variable contrast visible in CL lend insight into the mechanism controlling embayment formation (**Figure 6**). CL images of embayments in quartz were inspected carefully and categorized as having formed via growth, dissolution, or undetermined. Embayments likely formed during crystal growth were recognized by zone adaptations, deflected CL bands, and inward tapering of bands (e.g., Barbee et al., 2020). Embayments that may have formed via dissolution exhibited cross-cutting to dissected bands and smooth zone boundaries (e.g., Befus and Manga, 2019). To extend the reach of our CL analysis, we compiled our newly collected CL images (n = 17) with a collection of previously published CL images of quartz-hosted embayments (n = 161) (**Supplementary Figure S1**). From a collection of 182 embayments, 27% likely formed by growth and 45% by dissolution. The formation mechanism of the remaining 28% could not be determined from the images because of poor image quality or lack of clear banding in the embayment vicinity.

Embayments are filled with glass, bubbles, or combinations thereof. This filling character does not correspond to embayment size or morphology in any of the targeted eruptions. The filling character of quartz-hosted embayments can be categorized into four classifications: dense glass, intruding bubble, discrete bubbles, or devitrified (**Figures 3**, **7**). Dense embayments are fully filled with glass with no bubbles. Intruding bubbles continuously extend from the embayment interior into the vesiculated pumice external to the quartz crystal. This category has varying amounts of embayment glass. In some, a smaller bubble only partially fills the embayment, whereas others have a relatively large bubble that volumetrically dominates the embayment. The discrete bubbles category has isolated bubbles contained entirely within the embayment and the bubbles are

TABLE 3 | Observed bubble textural percentages.

Filling character	Bandelier Tuff	Tuff of Bluff point	Huckleberry ridge (F1-F3)	Giant pumice	Bishop Tuff (lg2Ea)	Mesa falls Tuff	Kos plateau Tuff	Bishop Tuff (F1-F3)	Oruanui Tuff	Younger Toba Tuff
Glassy	63	43	49	73	39	49	18	45	44	17
Intruded	15	12	39	20	31	41	29	37	48	33
Free-floating	12	11	3	2	28	3	19	13	5	22
Elongate	8	5	1	4	3	1	12	4	3	17
Devitrified	2	29	8	0	0	7	23	2	0	11
Embayed	85	82	71	69	55	53	49	37	34	4
N	678	597	526	279	877	530	453	432	616	1764

surrounded by glass. We identified two sub-categories of discrete bubbles: elongate and free-floating. Discrete, elongate bubbles are similar in shape to intruding bubbles but are distinguished by an isthmus of glass that fully isolates the bubble within the embayment's interior. These bubbles do not extend into vesiculated pumice exterior to the quartz's surface. Discrete, free-floating bubbles are spherical and are fully enclosed within embayment glass. Free-floating bubbles may be attached to crystal walls or entirely enveloped by glass. Here, we describe embayments that are partially modified by crystallization as "devitrified" embayments. These devitrified embayments are opaque, dark brown to black in color, and preserve no distinguishable bubble textures. Empty embayments are hollow cavities in the quartz host (e.g., Lava Creek Tuff examples from Befus and Manga, 2019). Empty embayments were recognized rarely across the targeted eruptions and were excluded from the characterization and counts. Across all eruptions, the dense glassy texture was the most common, followed by intruding bubbles and discrete, free-floating bubbles. We specify the diversity in bubble textures for each eruption in the follow subsections (**Table 3**, **Figure 8**).

Bandelier Tuff, Valles Caldera

Quartz crystals from the Valles caldera system were collected from the Tsankawi Pumice (RCE-B), the initial Plinian phase of the Upper Bandelier Tuff erupted at 1.14 Ma (Spell et al., 1990). The Tsankawi Pumice lies stratigraphically between the Tshirege and Cerro Toledo Formation. Tsankawi Pumice contains up to 30 vol% phenocrysts, primarily comprised of quartz and sanidine (Dunbar and Hervig, 1992). Quartz are predominantly euhedral, beta quartz bipyramids. Of all samples analyzed in this study, the Bandelier Tuff contained the greatest proportion of unfragmented grains. 85% of the quartz phenocrysts contain one or more embayments, which is the greatest abundance of embayed crystals across our suite of large silicic eruptions. Most of the embayments are glassy (62%). Bubble-bearing embayments are less common and we observe 15% have intruding bubbles, 12% have discrete, free-floating bubbles, 8% contain elongate bubbles, 2% are empty, and 2% are devitrified.

Oruanui Tuff, Taupo Caldera

The Oruanui Tuff is a quartz-poor rhyolite erupted at 26.5 ka (Liu et al., 2006). Whole-rock crystallinity in rhyolite samples from this eruption range from 3–13% (Wilson et al., 2006). The largest quartz in the Oruanui Tuff pumice samples were found in the 500–710 μm size fraction. Many crystals are highly fractured, but these were avoided when possible. Only 34% of quartz crystals were embayed. The population of quartz contains nearly equal proportions of dense glassy embayments and those with intruding bubbles, 44 and 48%, respectively. The remainder is 5% free-floating bubbles and 3% with elongate bubbles. No embayments were empty or devitrified. Two different eruptive units (F1 and F2) of the Oruanui Tuff were assessed independently to examine differences across eruptive pulses. Additionally, counts from two individual, whole pumice clasts from F1 collected at two different locations were chosen for comparison between individual pumice clasts and site localities. Embayment proportions were consistent between pumice clasts collected from separate sample locations, individual pumice clasts, and units. Counts from all units were thus combined and reported together.

Eruptions From Yellowstone Caldera

We examined embayment textures in three large-volume, pyroclastic eruptions from the Yellowstone caldera system. Airfall material was the source for quartz from the Huckleberry Ridge Tuff and Mesa Falls Tuff, whereas Tuff of Bluff Point quartz were extracted from pumice clasts from a loose, unwelded ignimbrite.

Quartz crystals from the Huckleberry Ridge Tuff contain fractures, but many have not fragmented. Huckleberry Ridge Tuff quartz are highly embayed with 71% of all crystals containing at least one embayment. Within the embayed group, dense glassy embayments and intruding bubbles dominate the observed textures, at 49% and 39%, respectively. When glassy, embayments commonly preserve a clear to light-yellow color gradient. Glass deep in the interior is the darkest shade, which becomes progressively less saturated towards the exterior. We see no correlation between bubble content, microlites, or glass color. Minor textures include discrete free-floating bubbles (3%), elongate bubbles (1%), and devitrified (8%). No empty embayments were observed. Sometimes Huckleberry Ridge Tuff embayments fully penetrate the interior of a crystal, meaning the embayment has at least two openings. This is

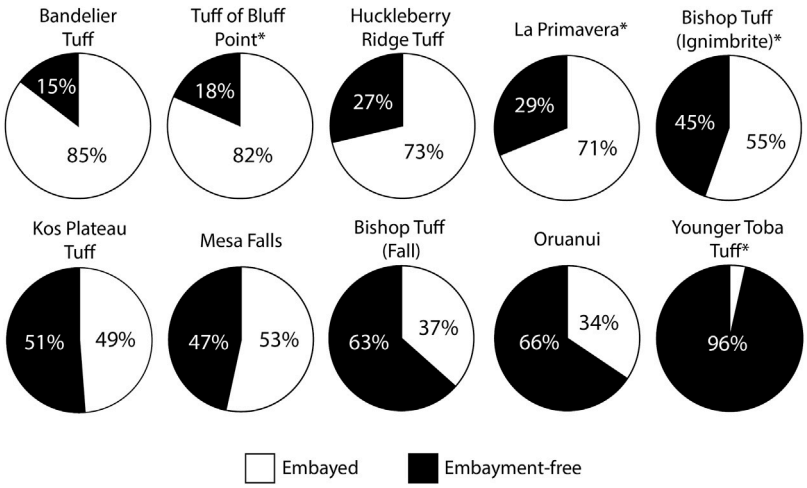

FIGURE 2 | Percentage of crystals with embayments from each eruption. Samples from ignimbrites are indicated with an asterisk.

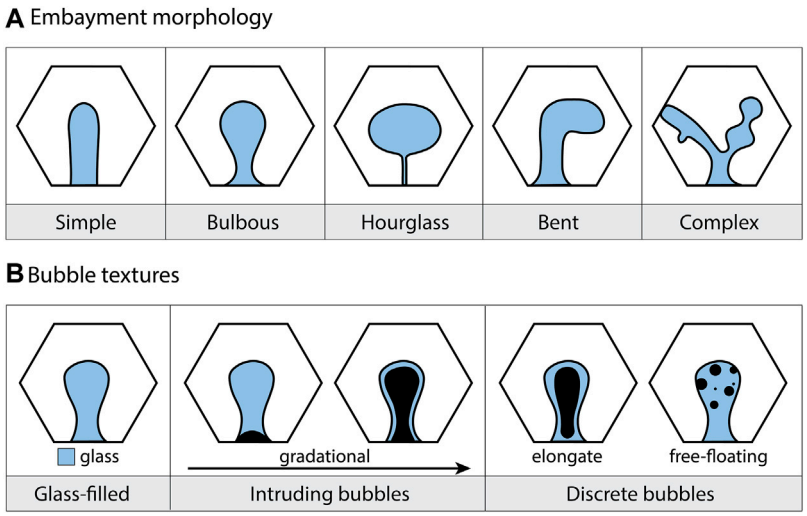

FIGURE 3 | Simplified schematic of **(A)** embayment morphologies, **(B)** idealized bubble textures, and associated naming system.

a rare morphology within our full suite samples (< 1%), but it occurs with unusual frequency in the Huckleberry Ridge Tuff quartz (5%).

The Mesa Falls Tuff contains large, euhedral, bipyramidal beta quartz. 53% of crystals examined contain at least one embayment. Dense, glassy embayments are the most common, accounting for 49% of observed textures. Like the Huckleberry Ridge Tuff, some dense glassy embayments from the Mesa Falls Tuff preserve color gradients. When found, these gradients tend to grade from yellow to brown. Intruding bubble textures are common, comprising 41% of the embayments. All other textures are infrequent, with 3% free-floating bubbles, 1% elongate bubbles, and 7% devitrified.

Quartz from the Tuff of Bluff Point are the second-most embayed population in our study suite, with 82% of crystals containing embayments. Tuff of Bluff Point quartz also commonly contain multiple embayment textures in single phenocrysts. The majority of embayments are dense glass (43%) that may be clear, brown, or have gradients from clear to brown. Bubbly textures are recognized in ~30% of the embayments, occurring as intruding bubbles (12%), free-floating bubbles (11%), and elongate bubbles (5%). The remaining ~30% of the embayments are opaque and devitrified. The abundance of devitrified embayments cannot solely be attributed to relatively slow post-eruptive cooling in an ignimbrite because some crystals host devitrified embayments immediately adjacent to dense, glassy embayments.

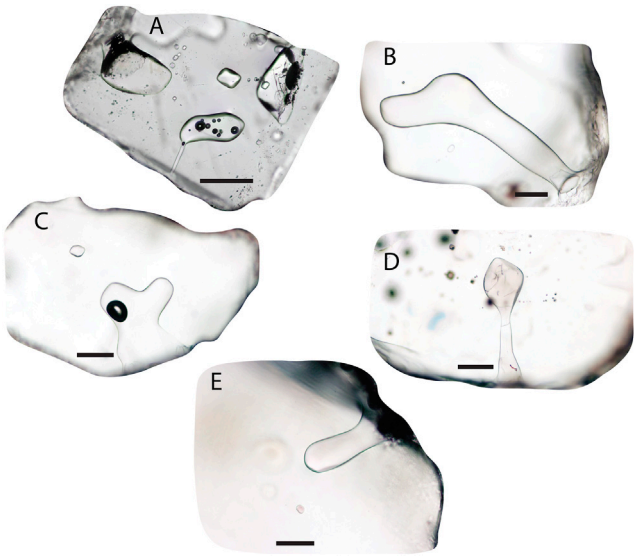

FIGURE 4 | Photomicrographs of embayment morphology classifications; **(A)** hourglass inclusion from the Bandelier Tuff (with discrete bubbles); **(B)** a bent embayment within the Kos Plateau Tuff; **(C)** complex embayment from the Kos Plateau Tuff (with a discrete bubble); **(D)** bulbous embayment in the Huckleberry Ridge Tuff; and **(E)** simple embayment from the Mesa Falls Tuff. Scale bar in each panel is 200 μm.

La Primavera

A single, 10-cm diameter pumice clast from the La Primavera Giant Pumice Horizon was crushed and picked for quartz. The Giant Pumice Horizon was emplaced by a subaqueous eruption within the La Primavera caldera (Sourisseau et al., 2020). Quartz phenocrysts in this unit are rare, rounded, and small. Most phenocrysts occurred in the 355–500 μm size fraction. Embayments are ubiquitous in the La Primavera quartz, appearing in 69% of the examined crystals. Embayments are notably clear, dense, and bubble-free. 73% of embayment textures are dense and glassy. Bubbles within embayment glass are less prevalent in this eruption, with only 20% containing intruding bubbles, 4% elongate bubbles, and 2% free-floating bubbles. No empty or devitrified embayments were observed.

Bishop Tuff, Long Valley Caldera

We assessed quartz-hosted embayments from pumice clasts from the Bishop Tuff's fall deposits and ignimbrite. Quartz from initial fall deposits F1-F3 have embayments in 37% of crystals. Approximately half of the embayments are dense glass (47%). Intruding bubbles comprise 37% of the remaining population, followed by free-floating (13%), elongate (4%), and devitrified (2%). Discrete, free-floating bubbles tend to occur as a single, isolated bubble rather than in clusters or multiples. Just over half of the quartz inspected from the Bishop Tuff Ignimbrite (Ig2Ea) sample contained embayments (55%). Of those, 39% of these were glassy, 31% contained intruding bubbles, free-floating bubbles followed closely with 28%, and elongate bubbles accounted for only 3% of total textures. No devitrified embayments were seen in the ignimbrite, but they were also rare in the fall deposits. Empty embayments were not observed in any Bishop Tuff samples.

Younger Toba Tuff, Toba Caldera

Blocks of welded Younger Toba Tuff ignimbrite were crushed and picked (sample was collected at Teles, stop 2.4 by S. Self during the 2018 IAVCEI field trip). Quartz in this sample is

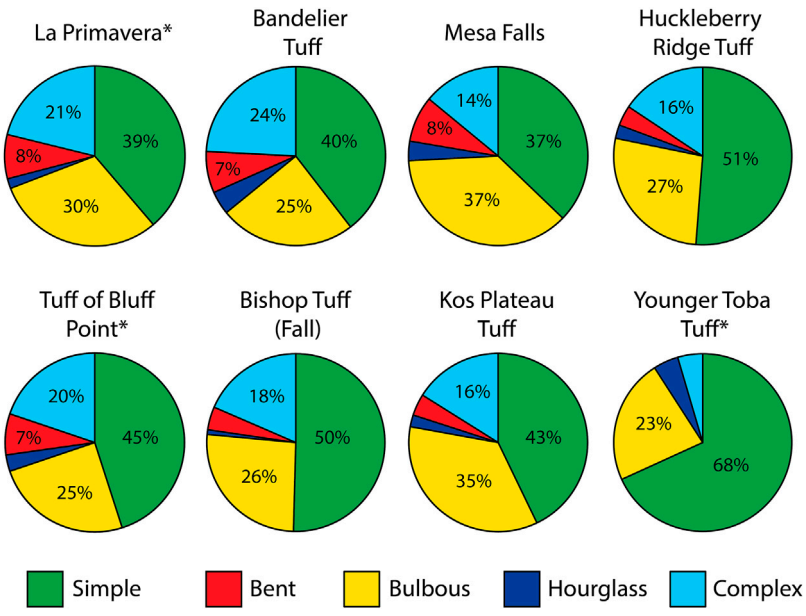

FIGURE 5 | Relative abundance of embayment morphologies. Samples from ignimbrites indicated with an asterisk.

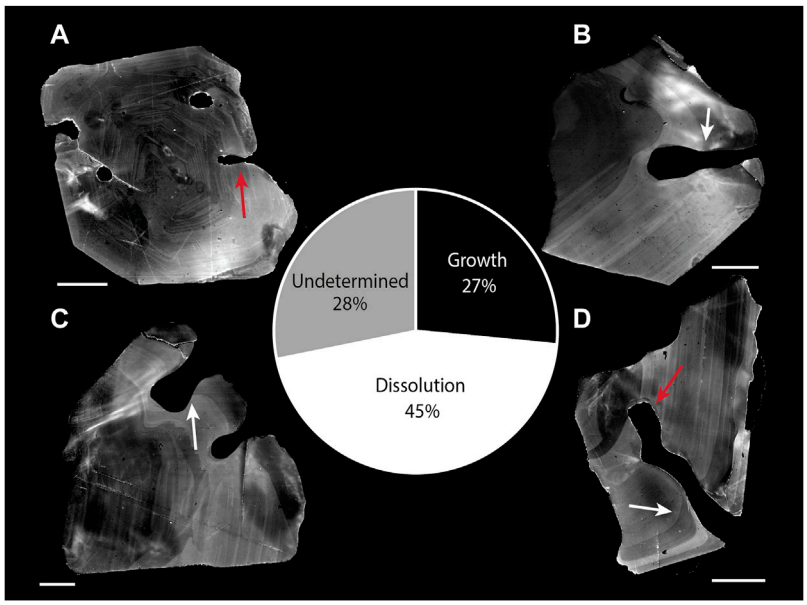

FIGURE 6 | Cathodoluminescence (CL) images of Bandelier Tuff **(A)** and Huckleberry Ridge Tuff quartz crystals **(B–D)**. Red arrows indicate dissected bands whereas white arrows indicate deflected CL bands. **(D)** quartz preserves periods of both growth and dissolution. Pie chart visualizes results from CL analysis of embayments in quartz prepared for this study and those compiled from the literature (n = 181 embayments). Scale bars are 200 μm.

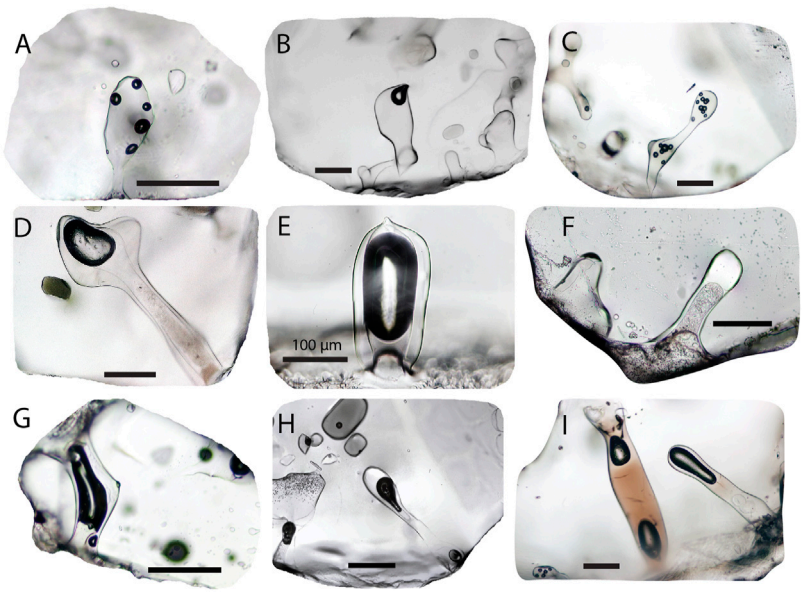

FIGURE 7 | Photomicrographs of embayment filling characteristic textures; discrete free-floating bubbles occurring in: **(A)** and **(C)** multiples and as a **(B)** single, lone bubble; **(D–F)** intruding bubbles which penetrate the full length of the embayment glass. Some index of refraction differences are complicated by mineral oil partially filling the intruding bubble. **(G–I)** discrete elongate bubbles which are similar to intruding bubbles, yet are discontinuous and truncate inside the embayment. Scale bar in each panel is 200 μm unless indicated otherwise **(E)**.

highly fragmented. Our counts from this eruption represent minimums as fragments may have contained additional embayments that are now lost. Embayments composed of dense, clear glass are rare (14%). Embayments from this eruption are more likely to contain bubbles than any other included in this study. Intruding bubbles accounting for 33% of observed textures, followed by discrete elongate (26%), free-floating (21%), and devitrified (5%).

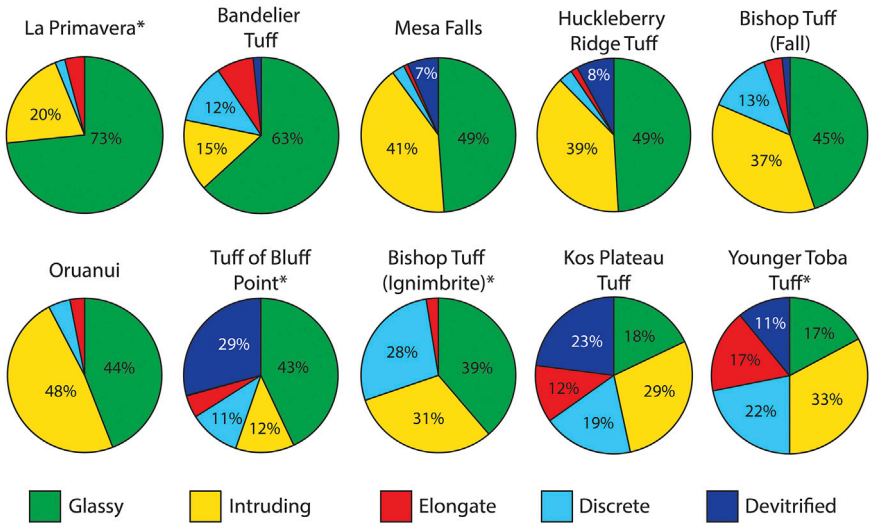

FIGURE 8 | Relative abundance of bubble textures within embayments. Samples from ignimbrites indicated with an asterisk.

The Kos Plateau Tuff, Aegean Arc

Pumice clasts from an unwelded ignimbrite from the Kos Plateau Tuff were gently crushed and picked for quartz phenocrysts. Quartz from this eruption were large, with some up to 2 mm across. Quartz is highly fractured and fragmented. Embayments in this eruption are prevalent, occurring in 51% of quartz crystals. Intruding bubbles are the dominant bubble texture (29%), followed by devitrified (23%), discrete free-floating (19%), dense glass (18%), and discrete elongate (12%).

DISCUSSION

Embayments are common features in quartz from large silicic eruptions. Nearly all quartz crystals are embayed in some eruptions (e.g., the Bandelier Tuff, Tuff of Bluff Point), whereas they are scarce in others (e.g., Younger Toba Tuff). Although the absolute abundance of embayed quartz varies by eruption, the diversity and proportions of embayment morphology is shared among all the studied units. We find the following consistent pattern of descending proportions: simple, bulbous, complex, bent, and hourglass. The most geometrically simple embayments occur the most commonly. The surfaces of most quartz-embayment contacts are smooth and curved. Only rare embayments preserve angular, faceted faces. When present, faceted embayment surfaces cover subordinate amounts of the total internal surface area.

Relict disequilibrium textures can be exploited using kinetics to extract meaningful timescales of magmatic processes (e.g., Watkins et al., 2012; Andrews and Befus 2020). The diffusion-limited volatile concentration gradients in embayment glass that can be used to estimate magmatic ascent rates are a significant and topical example (e.g., Liu et al., 2007; Myers et al., 2016; 2018; 2021). Here, the rounded quartz-embayment surfaces recognized in all of the large silicic eruptions may be a second timescale that records the duration between embayment formation and eruption. Rounded quartz surfaces will progressively facet as they grow and approach equilibrium crystal form (Gualda et al., 2012; Pamukcu et al., 2015). Using faceted to partially-faceted melt inclusions, Pamukcu et al. (2015) demonstrated that quartz grew over 10–600 years in the Oruanui Tuff, Ohakuri-Mamaku Tuff, and Bishop Tuff. The lowest energy geometry of quartz-embayment interfaces should also be faceted. Thus, rounded, unfaceted quartz-hosted embayments should begin to facet in < 100 years (Gualda et al., 2012; Pamukcu et al., 2015). This inference relies on the significant assumption that an embayment is a closed volume system that is not modified by melt crystallization (e.g., post entrapment crystallization). We recognize that our underlying assumption presents a considerable petrologic vulnerability, however, it is possible that the high viscosity, small volume interior of an embayment satisfies those criteria. If valid, the absence of faceting indicates the process that produces and maintains embayments could be active in the years to decades immediately preceding eruption.

Because the diversity and proportion of embayment morphologies are consistent across the ten eruptions considered here, we conclude there is a shared process that produces embayments in rhyolitic magmatic systems. Embayments have been interpreted in the past to form by crystal growth or dissolution, and there has been no community consensus. Those that favor a crystal growth mechanism attribute embayment forms to rapid, skeletal growth (e.g., Roedder, 1979; Loewen et al., 2017; Barbee et al., 2020). Others favor a dissolution mechanism produced when an exsolved volatile bubble attaches by surface tension to the quartz-melt interface, and subsequently drills into the phenocryst (Busby and Barker, 1966; Harris and Anderson, 1984; Donaldson and

Henderson, 1988; Befus and Manga, 2019). Embayments do commonly have a single, external bubble located at the crystal-melt interface. Volatile concentrations in and around such bubbles could produce local thermodynamic disequilibrium and enhance crystal dissolution (Busby and Barker, 1966).

The distribution and geometry of CL bands in quartz have been documented in many silicic eruptions (e.g., Liu et al., 2006; Peppard et al., 2001; Loewen and Bindeman, 2015; Pamukcu et al., 2015; 2016). Geometric superposition between CL bands and embayments may preserve sufficient crystallographic information to discern the formation mechanism of embayments. We assume that dissolution should produce crosscutting relationships with sharp, dissected bands. Following Barbee et al. (2020), a growth mechanism is assumed to produce deflected, inward tapering of CL bands. We applied our criteria to the collection of CL images of quartz intruded by various embayment morphologies. Dissolution is a common mechanism, accounting for 45% quartz-hosted embayments. Growth is also common, accounting for 27%. The formation mechanism for the remaining 28% could not be determined with confidence. Although both mechanisms are recognized in crystals from each eruption we studied, some are more common in certain eruptions. Dissolution is the primary mechanism in 67% of embayments in the Oruanui Tuff and 64% from the Bishop Tuff. No notable predominance occurs in other eruptions. We conclude that embayments form commonly via both dissolution and growth. Embayment formation is not always a simple binary in an eruption or even a single crystal. Some individual embayments even show evidence that they formed with episodes of both dissolution and growth. For example, embayments may sharply crosscut bands deep in crystal core, but CL bands nearer the exterior of the same crystal wrap and deflect towards the embayment (**Figure 6D**).

Glass and bubble textures preserved within embayments provide additional insight to the formation of embayments in the magma reservoir. Dense, glassy embayments are the most common filling texture in quartz from silicic eruptions. In 7 of the targeted eruptions they account for the largest proportion of embayments, occurring with proportions >50%. This result supports and lends credibility to embayment speedometry studies, because we confirm they are indeed an important and characteristic texture produced in magma reservoirs.

Bubbles in embayments are also common and have been observed within embayments from all eruptions studied herein. Quartz from some eruptions, like the Oruanui Tuff and Younger Toba Tuff, are dominated by bubbly embayments. Bubbles within embayments may be vestiges of pre-eruptive bubbles or form in response to supersaturation during magmatic ascent. Pre-eruptive bubbles have been shown to exist in many silicic systems (e.g., Wallace et al., 1995; Gualda and Anderson, 2007; Steele-MacInnis et al., 2017; Allison et al., 2021). For example, melt inclusions may contain pre-eruptive bubbles which are too large to have been formed solely via shrinkage during quench. Embayments contain bubbles that occupy up to 90 vol%. By comparison of large bubbles within embayments to those within inclusions, it is likely that some of the bubble-filled volume in embayments represents pre-eruptive, exsolved fluid. Intruding bubbles are the most common bubble texture. Because intruding bubbles extend from the external melt into the embayment channel, they result from, or at least are modified by, bubble growth during decompression and conduit ascent.

Bubble sizes and number density reflect ascent rates and conditions (e.g., Toramaru, 2006; Hajimirza et al., 2021). Embayments almost always preserve low bubble number densities and sizes. Melt trapped in quartz-hosted embayments did not vesiculate in the same fashion as free melt in the conduit. The dense embayment glass preserves thermodynamic disequilibrium. Instead of exsolving, volatiles remained dissolved in the melt. Rhyolitic embayments have been observed to contain up to 5 wt% H_2O and 100s of ppm CO_2 (e.g., Liu et al., 2007; Myers et al., 2016, Myers et al., 2018, Myers et al., 2021). Such H_2O and CO_2 contents indicate volatile supersaturations <200 MPa (Liu et al., 2005). Experiments and classical nucleation theory demonstrate that bubble nucleation scales with both volatile supersaturation and surface tension (Gardner and Ketcham, 2011; Hajimirza et al., 2019). In crystal-free rhyolite, large supersaturations of 100–300 MPa are required for bubble nucleation (e.g., Mourtada-Bonnefoi and Laporte, 1999, 2002, 2004; Mangan and Sisson, 2000; Cluzel at al., 2008). Crystalline heterogeneities, nanolites, or microlites, significantly reduce the impediment to nucleation imposed by surface tension, allowing nucleation at supersaturations less than a few 10s of MPa (Hurwitz and Navon, 1994). The elevated volatile contents, and supersaturations, preserved in embayments are in line with values associated with homogenous nucleation conditions. Furthermore, as dissolved H_2O content remains elevated in the melt embayment, decompression induced crystallization of microlites is suppressed. Indeed, microlites are exceedingly rare in embayment glass. We predict nanolites would also be rare. However, they have not been examined in embayments to date (e.g., Di Genova et al., 2018).

We were unable to identify any further possible causes for volatile supersaturation. To suppress bubble nucleation and growth, melt within embayments must experience a different environment than free melt in the conduit. Many parameters or conditions should act to reduce or eliminate this disequilibrium. Spatially, embayment melt is microns from the free melt and consequently they experience identical external variables like temperature. In addition, embayment melt is in chemical and physical communication with free melt in the conduit via the embayment channel. Because pressure is conveyed at the speed of sound in a fluid, the channel provides a fluid dynamic pathway to maintain near-instantaneous barometric equilibrium between melt in the embayment and the conduit (Gu et al., 2021). Unlike in a melt inclusion, overpressure cannot be sustained in the embayment interior. We conclude that bubble nucleation and growth is primarily suppressed by maintenance of relatively high surface tension in the embayment environment. As a result, magmatic volatile contents are preserved during ascent, and can only be lowered *via* diffusive equilibration.

Implications

Embayments are clocks that record eruptive timescales. Embayment speedometry is becoming a well-established technique and has seen its application grow significantly in the past 20 years. Embayments record magmatic decompression in the diffusion-limited volatile gradients preserved within dense, glassy embayments. These concentration profiles recover final ascent timescales on the order of minutes to hours. Additional disequilibrium textures are preserved in embayments. Rounded, unfaceted embayments may record the time from their formation leading up to eruption. This timescale may be shorter than that required for faceting, on the order of years to decades prior to eruption. Bubble textures, and lack thereof, may reveal a third timescale related by differences between homogenous and heterogenous nucleation. Although our analysis clarifies some behavior of melt and vesicles in embayments, it does not fully describe embayment processes. We do not attempt to explain why microlites do not form as readily inside of embayments. Nor do we explain why a single crystal sometimes preserves a range in bubble volumes in multiple embayments. Our textural assessment of natural embayments provides a useful framework for improving our understanding of embayments, and one that can help future studies further explore and exploit the record preserved in embayments.

DATA AVAILABILITY STATEMENT

The original contributions presented in the study are included in the article/**Supplementary Material**, further inquiries can be directed to the corresponding author.

AUTHOR CONTRIBUTIONS

AR led the primary sample collection, data analysis, and study design. KB assisted with sample collection, design, and analysis. AR and KB processed samples and performed statistical analyses. JT conducted numerical modeling. BA collected CL images. All authors contributed to the manuscript revision, read, and approved the submitted version.

FUNDING

This work was funded by NSF EAR 2015255 to KB and a GSA student grant to AR.

ACKNOWLEDGMENTS

We thank Madison Myers, Megan Saalfeld, Giovanni Sosa, Steve Self, Nick Meszaros, and Joe Dufek for sharing quartz-bearing pumice samples. We are grateful to Rebecca deGraffenried and Alison C. Rust for their insightful and constructive reviews. Thanks also to Jacob B. Lowenstern for editorial handling.

SUPPLEMENTARY MATERIAL

The Supplementary Material for this article can be found online at: https://www.frontiersin.org/articles/10.3389/feart.2021.742895/full#supplementary-material

REFERENCES

Allison, C. M., Roggensack, K., and Clarke, A. B. (2021). Highly Explosive Basaltic Eruptions Driven by CO2 Exsolution. *Nat. Commun.* 12 (1), 217–310. doi:10.1038/s41467-020-20354-2

Anderson, A. T. (1991). Hourglass Inclusions: Theory and Application to the Bishop Rhyolitic Tuff. *Am. Mineral.* 76 (3-4), 530–547.

Anderson, A. T. (2006). Bubbleless Glass Pockets and Natural Bubble Nucleation in Rhyolitic Magma. *AGU Fall Meet. Abstr.* 2006, V43A–V1785.

Andrews, B. J., and Befus, K. S. (2020). Supersaturation Nucleation and Growth of Plagioclase: a Numerical Model of Decompression-Induced Crystallization. *Contrib. Mineralogy Petrology.* 175 (3), 1–20. doi:10.1007/s00410-020-1660-9

Bachmann, O., Charlier, B. L. A., and Lowenstern, J. B. (2007). Zircon Crystallization and Recycling in the Magma Chamber of the Rhyolitic Kos Plateau Tuff (Aegean Arc). *Geol.* 35 (1), 73–76. doi:10.1130/g23151a.1

Barbee, O., Chesner, C., and Deering, C. (2020). Quartz Crystals in Toba Rhyolites Show Textures Symptomatic of Rapid Crystallization. *Am. Mineral. J. Earth Planet. Mater.* 105 (2), 194–226. doi:10.2138/am-2020-6947

Befus, K. S., and Manga, M. (2019). Supereruption Quartz Crystals and the Hollow Reentrants. *Geology.* 47, 710–714. doi:10.1130/G46275.1

Busby, T. S., and Barker, J. (1966). Simulative Studies of Upward Drilling. *J. Am. Ceram. Soc.* 49 (8), 441–446. doi:10.1111/j.1151-2916.1966.tb15413.x

Cashman, K. V., and Rust., A. (2016). *Causes and Implications of Suppressed Vesiculation and Crystallization in Phenocryst Embayments*. AGU Fall Meeting Abstracts 2016, V13G–02.

Cashman, K. V. (1992). Groundmass Crystallization of Mount St. Helens Dacite, 1980?1986: a Tool for Interpreting Shallow Magmatic Processes. *Contr. Mineral. Petrol.* 109, 431–449. doi:10.1007/BF00306547

Castro, J. M., and Dingwell, D. B. (2009). Rapid Ascent of Rhyolitic Magma at Chaitén Volcano, Chile. *Nature* 461 (7265), 780–783.

Castro, J. M., Dingwell, D. B., Cashman, K., Bachmann, O., Castro, J. M., and Dingwell, D. B. (2018). Rapid Ascent of Rhyolitic Magma at Chaitén Volcano, ChileRapid Ascent of Rhyolitic Magma at Chaitén Volcano, Chile. *Nat. communicationsNature.* 9461 (1), 1780–16783. doi:10.1038/nature08458

Castro, J. M., and Gardner, J. E. (2008). Did Magma Ascent Rate Control the Explosive-Effusive Transition at the Inyo Volcanic Chain, California. *Geol.* 36, 279. doi:10.1130/G24453A.1

Christiansen, R. L. (2001). *The Quaternary and Pliocene Yellowstone Plateau Volcanic Field of Wyoming, Idaho, and Montana*, 729. US Department of the Interior, US Geological Survey.

Cluzel, N., Laporte, D., Provost, A., and Kannewischer, I. (2008). Kinetics of Heterogeneous Bubble Nucleation in Rhyolitic Melts: Implications for the Number Density of Bubbles in Volcanic Conduits and for Pumice Textures. *Contrib. Mineral. Petrol.* 156 (6), 745–763. doi:10.1007/s00410-008-0313-1

deGraffenried, R. L., and Shea, T. (2021). Using Volatile Element Concentration Profiles in Crystal-Hosted Melt Embayments to Estimate Magma Decompression Rate: Assumptions and Inherited Errors. *Geochem. Geophys. Geosystems.* 22 (5), e2021GC009672. doi:10.1029/2021gc009672

Di Genova, D., Caracciolo, A., and Kolzenburg, S. (2018). Measuring the Degree of "Nanotilization" of Volcanic Glasses: Understanding Syn-Eruptive Processes Recorded in Melt Inclusions. *Lithos.* 318-319, 209–218. doi:10.1016/j.lithos.2018.08.011

Donaldson, C. H., and Henderson, C. M. B. (1988). A New Interpretation of Round Embayments in Quartz Crystals. *Mineral. Mag.* 52 (364), 27–33. doi:10.1180/minmag.1988.052.364.02

Dunbar, N. W., and Hervig, R. L. (1992). Volatile and Trace Element Composition of Melt Inclusions From the Lower Bandelier Tuff: Implications for Magma

Chamber Processes and Eruptive Style. *J. Geophys. Res.* 97 (B11), 15151–15170. doi:10.1029/92jb01340

Ferguson, D. J., Gonnermann, H. M., Ruprecht, P., Plank, T., Hauri, E. H., Houghton, B. F., et al. (2016). Magma Decompression Rates during Explosive Eruptions of Kīlauea Volcano, Hawaii, Recorded by Melt Embayments. *Bull. Volcanol.* 78, 71. doi:10.1007/s00445-016-1064-x

Gardner, J. E., and Ketcham, R. A. (2011). Bubble Nucleation in Rhyolite and Dacite Melts: Temperature Dependence of Surface Tension. *Contrib. Mineral. Petrol.* 162 (5), 929–943. doi:10.1007/s00410-011-0632-5

Gardner, J. E., Llewellin, E. W., Watkins, J. M., and Befus, K. S. (2017). Formation of Obsidian Pyroclasts by Sintering of Ash Particles in the Volcanic Conduit. *Earth Planet. Sci. Lett.* 459, 252–263. doi:10.1016/j.epsl.2016.11.037

Georgeais, G., Koga, K. T., Moussallam, Y., and Rose-Koga, E. F. (2021). Magma Decompression Rate Calculations With EMBER: A User-Friendly Software to Model Diffusion of H2O, CO2 and S in Melt Embayments. *Geochem. Geophys. Geosystems.* 22 (7), e2020GC009542. doi:10.7185/gold2021.5660

Gu, J. T., Fu, S., Gardner, J. E., Yamashita, S., Okuchi, T., and Lin, J.-F. (2021). Nonlinear Effects of Hydration on High-Pressure Sound Velocities of Rhyolitic Glasses. *Am. Mineral. J. Earth Planet. Mater.* 106 (7), 1143–1152. doi:10.2138/am-2021-7597

Gualda, G. A., and Anderson, A. T. (2007). Magnetite Scavenging and the Buoyancy of Bubbles in Magmas. Part 1: Discovery of a Pre-Eruptive Bubble in Bishop Rhyolite. *Contrib. to Mineral. Petrol.* 153 (6), 733–742.

Gualda, G. A. R., Pamukcu, A. S., Ghiorso, M. S., Anderson, A. T., Jr, Sutton, S. R., and Rivers, M. L. (2012). Timescales of Quartz Crystallization and the Longevity of the Bishop Giant Magma Body. *PloS one.* 7 (5), e37492. doi:10.1371/journal.pone.0037492

Hajimirza, S., Gonnermann, H. M., Gardner, J. E., and Giachetti, T. (2019). Predicting Homogeneous Bubble Nucleation in Rhyolite. *J. Geophys. Res. Solid Earth* 124 (3), 2395–2416.

Hajimirza, S., Gonnermann, H. M., and Gardner, J. E. (2021). Reconciling Bubble Nucleation in Explosive Eruptions With Geospeedometers. *Nat. Commun.* 12, 283. doi:10.1038/s41467-020-20541-1

Hammer, J. E., and Rutherford, M. J. (2002). An Experimental Study of the Kinetics of Decompression-Induced Crystallization in Silicic Melt. *J.Geophys. Res. Solid Earth.* 107 (B1), ECV–8. doi:10.1029/2001jb000281

Harris, D. M., and Anderson, A. T. (1984). Volatiles H2O, CO2, and Cl in a Subduction Related basalt. *Contrib. Mineral. Petrol.* 87 (2), 120–128. doi:10.1007/bf00376218

Humphreys, M. C. S., Menand, T., Blundy, J. D., and Klimm, K. (2008). Magma Ascent Rates in Explosive Eruptions: Constraints From H2O Diffusion in Melt Inclusions. *Earth Planet. Sci. Lett.* 270, 25–40. doi:10.1016/j.epsl.2008.02.041

Hurwitz, S., and Navon, O. (1994). Bubble Nucleation in Rhyolitic Melts: Experiments at High Pressure, Temperature, and Water Content. *Earth Planet. Sci. Lett.* 122 (3-4), 267–280. doi:10.1016/0012-821x(94)90001-9

Liu, Y., Anderson, A. T., Wilson, C. J. N., Davis, A. M., and Steele, I. M. (2006). Mixing and Differentiation in the Oruanui Rhyolitic Magma, Taupo, New Zealand: Evidence from Volatiles and Trace Elements in Melt Inclusions. *Contrib. Mineral. Petrol.* 151 (1), 71–87. doi:10.1007/s00410-005-0046-3

Liu, Y., Anderson, A. T., and Wilson, C. J. N. (2007). Melt Pockets in Phenocrysts and Decompression Rates of Silicic Magmas Before Fragmentation. *J. Geophys. Res.* 112, B06204. doi:10.1029/2006JB004500

Liu, Y., Zhang, Y., and Behrens, H. (2005). Solubility of H2O in Rhyolitic Melts at Low Pressures and a New Empirical Model for Mixed H2O–CO2 Solubility in Rhyolitic Melts. *J. Volcanology Geothermal Res.* 143 (1-3), 219–235. doi:10.1016/j.jvolgeores.2004.09.019

Lloyd, A. S., Ruprecht, P., Hauri, E. H., Rose, W., Gonnermann, H. M., and Plank, T. (2014). NanoSIMS Results From Olivine-Hosted Melt Embayments: Magma Ascent Rate During Explosive Basaltic Eruptions. *J. Volcanology Geothermal Res.* 283, 1–18. doi:10.1016/j.jvolgeores.2014.06.002

Loewen, M. W., and Bindeman, I. N. (2015). Oxygen Isotope and Trace Element Evidence for Three-Stage Petrogenesis of the Youngest Episode (260–79 ka) of Yellowstone Rhyolitic Volcanism. *Contrib. to Mineral. Petrol.* 170 (4), 1–25.

Loewen, M. W., Bindeman, I. N., and Melnik, O. E. (2017). Eruption Mechanisms and Short Duration of Large Rhyolitic Lava Flows of Yellowstone. *Earth Planet. Sci. Lett.* 458, 80–91. doi:10.1016/j.epsl.2016.10.034

Lowenstern, J. B. (2003). Melt Inclusions Come of Age: Volatiles, Volcanoes, and Sorby's Legacy. *Dev. Volcanology.* 5, 1–21. doi:10.1016/S1871-644X(03)80021-9

Mangan, M., and Sisson, T. (2000). Delayed, Disequilibrium Degassing in Rhyolite Magma: Decompression Experiments and Implications for Explosive Volcanism. *Earth Planet. Sci. Lett.* 183 (3-4), 441–455. doi:10.1016/s0012-821x(00)00299-5

Mourtada-Bonnefoi, C. C., and Laporte, D. (1999). Experimental Study of Homogeneous Bubble Nucleation in Rhyolitic Magmas. *Geophys. Res. Lett.* 26 (23), 3505–3508. doi:10.1029/1999GL008368

Mourtada-Bonnefoi, C. C., and Laporte, D. (2002). Homogeneous Bubble Nucleation in Rhyolitic Magmas: an Experimental Study of the Effect of H2O and CO2. *J. Geophys. Res. Solid Earth.* 107 (B4), ECV–2. doi:10.1029/2001JB000290

Mourtada-Bonnefoi, C. C., and Laporte, D. (2004). Kinetics of Bubble Nucleation in a Rhyolitic Melt: an Experimental Study of the Effect of Ascent Rate. *Earth Planet. Sci. Lett.* 218 (3-4), 521–537. doi:10.1016/s0012-821x(03)00684-8

Moussallam, Y., Rose-Koga, E. F., Koga, K. T., Médard, E., Bani, P., Devidal, J.-L., et al. (2019). Fast Ascent Rate During the 2017-2018 Plinian Eruption of Ambae (Aoba) Volcano: a Petrological Investigation. *Contrib. Mineral. Petrol.* 174, 90. doi:10.1007/s00410-019-1625-z

Myers, M. L., Druitt, T. H., Schiavi, F., Gurioli, L., and Flaherty, T. (2021). Evolution of Magma Decompression and Discharge During a Plinian Event (Late Bronze-Age Eruption, Santorini) from Multiple Eruption-Intensity Proxies. *Bull. Volcanol.* 83, 18. doi:10.1007/s00445-021-01438-3

Myers, M. L., Wallace, P. J., Wilson, C. J. N., Morter, B. K., and Swallow, E. J. (2016). Prolonged Ascent and Episodic Venting of Discrete Magma Batches at the Onset of the Huckleberry Ridge Supereruption, Yellowstone. *Earth Planet. Sci. Lett.* 451, 285–297. doi:10.1016/j.epsl.2016.07.023

Myers, M. L., Wallace, P. J., Wilson, C. J. N., Watkins, J. M., and Liu, Y. (2018). Ascent Rates of Rhyolitic Magma at the Onset of Three Caldera-Forming Eruptions. *Am. Mineral.* 103, 952–965. doi:10.2138/am-2018-6225

Newcombe, M. E., Plank, T., Barth, A., Asimow, P. D., and Hauri, E. (2020). Water-in-olivine Magma Ascent Chronometry: Every crystal Is a Clock. *J. Volcanology Geothermal Res.* 398, 106872. doi:10.1016/j.jvolgeores.2020.106872

Pamukcu, A. S., Gualda, G. A. R., Bégué, F., and Gravley, D. M. (2015). Melt Inclusion Shapes: Timekeepers of Short-Lived Giant Magma Bodies. *Geology.* 43, 947–950. doi:10.1130/G37021.1

Pamukcu, A. S., Ghiorso, M. S., and Gualda, G. A. (2016). High-Ti, Bright-CL Rims in Volcanic Quartz: A Result of Very Rapid Growth. *Contrib. to Mineral. Petrol.* 171 (12), 1–9.

Peppard, B. T., Steele, I. M., Davis, A. M., Wallace, P. J., and Anderson, A. T. (2001). Zoned Quartz Phenocrysts from the Rhyolitic Bishop Tuff. *Am. Mineral.* 86 (9), 1034–1052. doi:10.2138/am-2001-8-910

Rivera, T. A., Schmitz, M. D., Jicha, B. R., and Crowley, J. L. (2016). Zircon Petrochronology and 40Ar/39Ar Sanidine Dates for the Mesa Falls Tuff: Crystal-Scale Records of Magmatic Evolution and the Short Lifespan of a Large Yellowstone Magma Chamber. *J. Petrology.* 57 (9), 1677–1704. doi:10.1093/petrology/egw053

Roedder, E. (1979). Origin and Significance of Magmatic Inclusions. *bulmi.* 102 (5), 487–510. doi:10.3406/bulmi.1979.7299

Rust, A., and Cashman, K. (2017). "Interpretations of Phenocryst Embayments," in EGU General Assembly Conference Abstracts, 17887.

Rutherford, M. J. (2008). Magma Ascent Rates. *Rev. Mineralogy Geochem.* 69, 241–271. doi:10.2138/rmg.2008.69.7

Saalfeld, M. A., Myers, M., and Waelkens, C. M. (2019). Conduit Controls on the Release of Material at the Onset of Two Caldera-Forming Eruptions: Case Study from the Bandelier Tuff. *AGU Fall Meet. Abstr.* 2019, V51F.

Sourisseau, D., Macías, J. L., García Tenorio, F., Avellán, D. R., Saucedo Girón, R., Bernal, J. P., et al. (2020). New Insights Into the Stratigraphy and 230Th/U Geochronology of the Post-Caldera Explosive Volcanism of La Primavera Caldera, Mexico. *J. South Am. Earth Sci.* 103, 102747. doi:10.1016/j.jsames.2020.102747

Spell, T. L., Harrison, T. M., and Wolff, J. A. (1990). 40Ar/39Ar Dating of the Bandelier Tuff and San Diego Canyon Ignimbrites, Jemez Mountains, New Mexico: Temporal Constraints on Magmatic Evolution. *J. Volcanology Geothermal Res.* 43 (1-4), 175–193. doi:10.1016/0377-0273(90)90051-g

Steele-MacInnis, M., Esposito, R., Moore, L. R., and Hartley, M. E. (2017). Heterogeneously Entrapped, Vapor-Rich Melt Inclusions Record Pre-Eruptive Magmatic Volatile Contents. *Contrib. Mineral. Petrol.* 172 (4), 18. doi:10.1007/s00410-017-1343-3

Toramaru, A. (2006). BND (Bubble Number Density) Decompression Rate Meter for Explosive Volcanic Eruptions. *J. Volcanology Geothermal Res.* 154, 303–316. doi:10.1016/j.jvolgeores.2006.03.027

Toramaru, A., Noguchi, S., Oyoshihara, S., and Tsune, A. (2008). MND(Microlite Number Density) Water Exsolution Rate Meter. *J. Volcanology Geothermal Res.* 175, 156–167. doi:10.1016/j.jvolgeores.2008.03.035

Wallace, P. J., Anderson, A. T., and Davis, A. M. (1995). Quantification of Pre-Eruptive Exsolved Gas Contents in Silicic Magmas. *Nature.* 377 (6550), 612–616. doi:10.1038/377612a0

Watkins, J. M., Manga, M., and DePaolo, D. J. (2012). Bubble Geobarometry: A Record of Pressure Changes, Degassing, and Regassing at Mono Craters, California. *Geology.* 40 (8), 699–702. doi:10.1130/g33027.1

Wilson, C. J. N., Blake, S., Charlier, B. L. A., and Sutton, A. N. (2006). The 26·5 Ka Oruanui Eruption, Taupo Volcano, New Zealand: Development, Characteristics and Evacuation of a Large Rhyolitic Magma Body. *J. Petrology.* 47 (1), 35–69. doi:10.1093/petrology/egi066

Conflict of Interest: The authors declare that the research was conducted in the absence of any commercial or financial relationships that could be construed as a potential conflict of interest.